Dynamic Segmentation of Grey-Scale Images in a Computer Model of the Mammalian Retina

Garrett T. Kenyon[*a,c], Neal R. Harvey [b,c], Gregory J. Stephens [a,c] and James Theiler [b,c]

[a]P-21, MS D454, Biological and Quantum Physics
[b]ISR-2, MS B244, Space and Remote Sensing Sciences
[c]Los Alamos National Laboratory, Los Alamos, NM, 87545, USA

ABSTRACT

Biological studies suggest that neurons in the mammalian retina accomplish a dynamic segmentation of the visual input. When activated by large, high contrast spots, retinal spike trains exhibit high frequency oscillations in the upper gamma band, between 60 to 120 Hz. Despite random phase variations over time, the oscillations recorded from regions responding to the same spot remain phase locked with zero lag whereas the phases recorded from regions activated by separate spots rapidly become uncorrelated. Here, a model of the mammalian retina is used to explore the segmentation of high contrast, gray-scale images containing several well-separated objects. Frequency spectra were computed from lumped spike trains containing 2×2 clusters of neighboring retinal output neurons. Cross-correlation functions were computed between all cell clusters exhibiting significant peaks in the upper gamma band. For each pair of oscillatory cell clusters, the cross-correlation between the lumped spike trains was used to estimate a functional connectivity, given by the peak amplitude in the upper gamma band of the associated frequency spectra. There was a good correspondence between the largest eigenvalues/eigenvectors of the resulting sparse functional connectivity matrix and the individual objects making up the original image, yielding an overall segmentation comparable to that generated by a standard watershed algorithm.

Keywords: synchrony, gamma oscillations, phase locking, temporal code, rate code

1. INTRODUCTION

Ganglion cells — the output neurons of the retina — represent local stimulus properties, such as contrast, as changes in their firing rates. In addition, ganglion cells may encode global stimulus properties, such as connectedness, via coherent oscillations. Large stimuli can evoke high frequency oscillatory potentials (HFOPs) in mammalian retinas at frequencies between 60-120 Hz[1-6] and similar oscillations have been recorded in cold-blooded vertebrates at lower frequencies[7, 8]. HFOPs are also present in electroretinograms (ERGs) of humans[9, 10] and other primates[11, 12]. The phylogenetic conservation of HFOPs across vertebrate retinas suggests they may be important for visual function.

In those retinal preparations where the phase-locking behavior of retinal oscillations has been directly investigated, primarily in the frog[7] and cat[4], HFOPs have been shown to be stimulus-specific. Oscillations arising from regions activated by the same contiguous patch of illumination are phase locked with approximately zero lag, even though the phase itself varies randomly over time relative to the stimulus onset. The oscillations evoked by spatially separate patches, however, do not remain phase locked and thus the signals arising from such regions rapidly become uncorrelated.

Based on initial results from a linear model of the inner retina, we proposed that negative feedback from axon-bearing amacrine cells—inhibitory inter-neurons—produces oscillatory responses that might underlie HFOPs[13]. According to this hypothesis, the dendrites of axon-bearing amacrine cells are excited by neighboring ganglion cells via electrical synapses, or gap junctions, whereas their axons provide feedback inhibition to more distant ganglion cells.

[*] gkenyon@lanl.gov; phone 1 505 667-1900; fax 1 505 665-4507

This connectivity is consistent with patterns of ganglion cell tracer coupling in the cat and primate retinas[14-16], as well as with electron microscopy of gap junction contacts between ganglion and amacrine cells[15] and with the distribution of synaptic contacts made by wide-field amacrine cells[17, 18].

Subsequent modeling studies confirmed that axon-mediated feedback from spiking amacrine cells could produce physiologically realistic HFOPs consistent with the temporal dynamics and center-surround organization of cat retinal ganglion cells[19]. In these more realistic models, an integrate-and-fire process was used to describe the behavior of spiking neurons and a stochastic process to describe the effects of transmitter release from non-spiking neurons. Ganglion cells were modeled as cat alpha (Y) ganglion cells, based on physiological evidence that alpha ganglion cells fire synchronously[20, 21]. The axon-mediated HFOPs observed in these studies were robust to changes in individual parameters and did not depend critically on the numerical precision of the integration routine[19].

Recently, we used the same integrate-and-fire model of the inner retina to characterize the stimulus-specificity of HFOPs produced by axon-mediated feedback[22]. The phase locking of retinal HFOPs produced by axon-mediated feedback did not depend critically on the distance between the recorded cells but on whether there existed a continuously stimulated path between them (i.e. whether the corresponding points in the image belonged to a single, contiguous patch). Phase locking fell off abruptly as the end-to-end distance, or gap, between two narrow bar stimuli was increased, illustrating the pivotal role of nearest-neighbor electrical synapses in synchronizing HFOPs within contiguously activated regions. HFOPs were much less stimulus-specific for over-lapping objects separated by a long, low contrast border, such as commonly occurs in natural scenes. Nonetheless, our results indicated that retinal oscillations could provide a dynamic label for segmenting visual inputs into distinct regions, or patches, particularly for those portions of the scene consisting of high contrast, well-separated objects. However, in the above studies, the dynamic segmentation produced by the retinal model was only assessed implicitly by measuring firing correlations between a few carefully selected locations. Here, we employ a scene wide analysis that simultaneously takes into account firing correlations between all cell pairs, thus yielding an explicit segmentation of the visual input based on retinal oscillations.

The algorithm we used for dynamically segmenting gray scale images based on oscillatory retinal output was constructed as follows. Starting with the output of the retinal model, correlations were measured between all image locations possessing significant local oscillatory power. For this analysis, separate image locations were defined by non-overlapping 2×2 windows of neighboring ganglion cells. Individual correlation functions were Fourier transformed and the peak amplitude in the upper gamma band was used to estimate an effective connectivity between corresponding image locations. The effective connectivity between all pairs of output pixels was used to define a functional connectivity matrix. This matrix was sparse, both because the image used in our example consisted of only a few distinct objects and because matrix elements less than approximately half the maximum value were set identically to zero. To extract the segmentation information implicit in the functional connectivity matrix, the eigenvalues and eigenvectors were extracted. In our example, the eigenvectors associated with the largest eigenvalues corresponded closely to the individual objects in the scene.

The remainder of the paper is organized as follows. First, we present an overview of the retinal model and our analysis procedures, including the extraction of spectral information from lumped spike train data, the calculation of cross-correlation functions and the eigenvalue analysis of the resulting functional connectivity matrix. Second, we present the main results of our analysis for a particular image. Finally, we discuss the general implications of our results for the further development of biologically inspired image processing methods.

2. METHODS

2.1. Model Overview

The model retina consisted of five parallel, interconnected, 2-D grids, one for each cell type (fig. 1). The model bipolar cells produced excitatory postsynaptic potentials (EPSPs) in both ganglion cells and amacrine cells according to a random process[23]. EPSPs were balanced by inhibitory post-synaptic potentials, or IPSPs, from three different amacrine cell types encompassing three different spatial scales: 1) small amacrine cells whose dendritic fields were the same size as those of the bipolar cells, 2) large amacrine cells whose dendritic fields were the same size as those of the ganglion cells, and 3) axon-bearing amacrine cells, whose dendritic fields were the same size as those of the bipolar cells but whose axonal connections spread out over a large retinal area. Of the three amacrine cell types in the model, only the
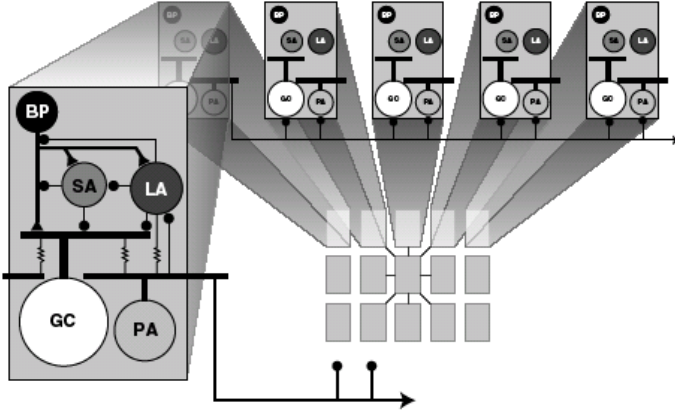
Fig. 1. Cell types and major connections in the retinal model illustrated at three spatial scales. The model consisted of a 128×128 array of identical local processing modules consisting of five cells types: bipolar (BP) cells, small (SA), large (LA) and poly-axonal (PA) amacrine cells, and alpha ganglion (GC) cells. In each local module, there were 4 BPs, 4 SAs, 4 PAs, 1 LA and 1 GC (only one cell of each type is depicted). *Local Connections*: The BPs excited all four 3rd order cell types, but their input to the PAs was very weak (not all connections depicted). Amacrine cells made three kinds of local inhibitory connections: Feed forward inhibition of the GCs, feedback inhibition of the BPs, and serial inhibition among themselves. The PAs were coupled by gap junctions to the GCs, the LAs, and to each other. *Long-Range Connections*: The PAs gave rise to long axons that inhibited all cell types in the surrounding area, but most strongly contacted the GCs and other PAs. Explanation of symbols: Excitation (triangles), inhibition (circles), gap junctions (resistors).

axon-bearing amacrine cells fired spikes. All three amacrine cell types made feedforward synapses onto ganglion cells, feedback synapses onto bipolar cells, as well as serial synapses among themselves.

2.2. Simulation

All cell types were modeled as single compartment, RC circuit elements obeying a first order differential equation of the following form:

$$\dot{\vec{V}}^{(k)} = -\frac{1}{\tau^{(k)}}\left(\vec{V}^{(k)} - b^{(k)} - \vec{L}^{(k)}\right)$$

$$+ \frac{1}{\tau^{(k)}}\left(\sum_{k'}\vec{W}^{(k,k')}\cdot f^{(k,k')}\left(\vec{V}^{(k')}\right)\cdot \vec{W}^{(k,k')^T}\right)$$

(1)

where $\{V^{(k)}\}$ is a 2-D array denoting the normalized membrane potentials of all cells of type k, $1 \le k \le 5$, $\tau^{(k)}$ are the time constants, $b^{(k)}$ are bias currents, $\{L^{(k)}\}$ are 2-D arrays representing light stimulation ($\{L^{(k)}\}=0$, $k \ne 1$), $\{W^{(k,k')}\}$ gives the connection strengths, implemented as Gaussian functions of the Euclidian distance between presynaptic, k', and postsynaptic, k, cell types, and the functions $f^{(k,k')}$ give the associated input-output relations. The weight matrices, $\{W^{(k,k')}\}$, and the input-output relations, $f^{(k,k')}$, are described in greater detail below. The output of

the axon-mediated inhibition was delayed by 2 msec, except for the axonal connections onto the axon-bearing amacrine cells, which was delayed for 1 msec. This difference in conduction delays resulted from limitations imposed by the original implementation of the simulator. Subsequent studies, using a more advanced simulator, confirmed that similar results to those reported here are obtained when a physiologically realistic model of axon conduction delays is employed[19]. All other synaptic interactions were delayed by one time step, equal to 1 msec, representing a typical rise-time for PSPs. Equations were integrated using a direct Euler method. Separate control studies confirmed that the model exhibited similar behavior regardless of the integration step size as long as the finite PSP rise time was modeled explicitly[19].

The input-output function for gap junctions was given by the identity:

$$f^{(k,k')}\left(\vec{V}^{(k')}\right) = \vec{V}^{(k')},$$

(2)

where the dependence on the presynaptic potential has been absorbed into the definition of $\tau^{(k)}$.

The input-output function for graded stochastic synapses, which did not require action potential spikes to produce PSPs, was constructed by comparing, on each time step, a random number with a Fermi-function:

$$f^{(k,k')}\left(\vec{V}^{(k')}\right) = \theta\left(\left[\frac{1}{1 + \exp\left(-\alpha\vec{V}^{(k')}\right)}\right] - r\right),$$

(3)

where α sets the gain (equal to 4), r is a uniform random deviate equally likely to take any real value between 0 and 1, and θ is a step function, $\theta(x) = 1$, $x > 0$; $\theta(x) = 0$, $x \le 0$.

Finally, the input-output relation used to describe the conventional synapses made by the spiking axon-bearing amacrine cells was:

$$f^{(k,k')}\left(\vec{V}^{(k')}\right) = \theta\left(\vec{V}^{(k')}\right).$$

(4)

A modified integrate-and-fire mechanism was used to model spike generation. A positive pulse (amplitude = 10.0) was delivered to the cell on the time step after the membrane potential crossed threshold, followed by a negative pulse (amplitude = -10.0) after a delay of 1 msec. It was necessary to explicitly model action potentials as these could affect neighboring cells via gap junctions. The bias current, b, was incremented by -0.5 following each spike, and then decayed back to the resting value with the time constant of the cell, representing a relative refractory period.

Synaptic weights were modeled as separable Gaussian functions, with the total weight given by the product of two terms representing the dependence on either the horizontal (columns) or vertical separation (rows) between pre- and post-synaptic elements. The horizontal weight factor, $\{W^{(k,k')}\}_{i(k),j(k')}$, was determined by a Gaussian function of the following form:

$$W^{(k,k')}_{i^{(k)},j^{(k')}} = \alpha\sqrt{W^{(k,k')}}\exp\left[-\frac{\left\|i^{(k)}-j^{(k')}\right\|^2}{2\sigma^{(k,k')^2}}\right] \tag{5}$$

which gives the synaptic weight between the presynaptic location $j^{(k')}$ (the jth column in the array of cells of type k') to the postsynaptic location $i^{(k)}$ (the ith column in the array of cells of type k), α is a normalization factor which ensured that the total integrated synaptic input equaled $W^{(k,k')}$, $\sigma^{(k,k')}$ is the Gaussian radius of the interaction, and the quantity $\|i^{(k)}-j^{(k')}\|$ denotes the horizontal distance between the pre- and post-synaptic columns, taking into account the wrap around boundary conditions employed to mitigate edge effects. An analogous weight factor describes the dependence on the row separation.

The spatial extent of synaptic interactions depended on the input and output radii of the post- and pre-synaptic cell types, respectively. Specifically, equation 5 was augmented by a cutoff condition that prevented synaptic interactions beyond a specified distance, determined by the radius of influence of the presynaptic outputs and the postsynaptic inputs, corresponding to the axonal and dendritic fields, respectively. A synaptic connection was only possible if the output radius of the presynaptic cell overlapped the input radius of the postsynaptic cell. Except for the long distance connections made by the axon-bearing amacrine cells, the input and output radii were equal, reflecting the fact that in the retina the same processes are often both pre- and post-synaptic. For the large amacrine cells and the ganglion cells, the radius of influence extended out to the centers of the nearest neighboring cells of the same type. The radii of the bipolar, small, and axon-bearing amacrine cells (non-axonal connections only) extended only halfway to the nearest cell of the same type. Explicit values for model parameters are listed in tables 1 and 2.

TABLE 1
CELLULAR PARAMETERS

	τ	b	n×n	d	σ
BP	10.0	−0.0	64×64	0.25	0.25
SA	25.0	−0.5	64×64	0.25	0.25
LA	20.0	−0.25	32×32	1.0	0.5
PA	5.0	−0.025	64×64	0.25/9.0[a]	0.25/3.0[a]
GC	5.0	−0.025	32×32	1.0	0.5

Table 1. Explanation of symbols: τ: time constant (msec); b: bias; n×n: array size; d: cutoff radius, σ: Gaussian radius (see eq. 5). [a]Inner radius/outer radius.

2.3. Spike Train Analysis

Spike trains 4.936 seconds in duration (the first 64 msec of simulated activity was not analyzed to avoid startup artifacts) were obtained either from single ganglion cells or from clusters of 4 neighboring ganglion cells arranged as non-overlapping 2×2 arrays. The single or multi-unit spike trains were analyzed as follows. *Mean firing rate*: Mean firing rates were determined by counting the number of spikes and normalizing by the length of the recording interval and by the number of cells included in the spike record. A binary firing rate mask was constructed by defining a threshold, equal to 3 standard deviations above the mean firing rate obtained by averaging over all spike trains across the entire image. *Gamma-band activity*: Spike trains were Fourier transformed and the peak spectral amplitude in the upper gamma band, 60-120 Hz, was determined. A binary gamma-band activity mask was constructed by defining a threshold, equal to 3 standard deviations above the mean gamma-band activity obtained by averaging over

TABLE 2
SYNAPTIC WEIGHTS

	L	BP	SA	LA	PA	GC
BP	3.0^a	*	-0.375^b	3.0^b	$-3.0^b/-15.0c$	*
SA	*	3.0^b	*	-3.0^b	$0.0^b/-15.0^c$	*
LA	*	3.0^b	*	0.25^a	$-3.0^a/-15.0^c$	*
PA	*	0.75^b	$-0.75b$	0.25^a	$0.25^a/-45.0^c$	0.25^a
GC	*	9.0^b	$-4.5b$	-4.5^b	$0.25^a/-270.0^c$	*

Table 2. Each term represents the total integrated weight (the quantity $W^{(i,i')}$ in eq. 5) from all synapses arising from the corresponding presynaptic type (columns) to each cell of the corresponding postsynaptic type (rows). The first column, labeled L, denotes connections made by the external stimulus. Asterisks (*) indicate the absence of a corresponding connection. Synapse type indicated by superscript: [a]gap junction, [b]graded synapse, [c]conventional synapse. [d]Maximum coupling efficiency (ratio of post- to pre-synaptic depolarization) for this gap junction synapse: DC=11.3%, Action Potential=2.7%.

all spike trains. Gamma-band activity was only evaluated for the multi-unit spike trains.

For all image locations exceeding the gamma-band activity threshold, cross-correlation histograms (CCHs) were computed between all pairs of multi-unit spike trains and the result expressed as a fraction of the baseline correlation amplitude due to chance. Typically, correlations between spike trains drawn from different stimulus trials (shift predictors) are subtracted to eliminate the contribution from stimulus coordination[24]. However, this manipulation was not necessary for the long, stationary spike trains analyzed here. CCHs were plotted as a function of the delay after averaging over all events occurring during the analyzed portion of the response (64-5,000 msec). For each delay value, this average was compensated for edge effects arising from the finite length of the two spike trains (lag corrected). All rate and correlation measures used a bin width of 1 msec.

To obtain a functional connectivity matrix, the individual CCHs were Fourier analyzed and the peak spectral amplitude in the upper gamma-band was determined. Whenever the gamma-band oscillations at two image locations were strongly phase locked, there was pronounced periodic structure their CCH and thus a pronounced peak in the corresponding frequency spectra in the upper gamma band. On the other hand, for image locations whose oscillations were not phase locked, the CCH was essentially flat and the peak spectral amplitude in the upper gamma band was negligible. The peak spectral amplitude in the CCH, computed between all image locations exhibiting significant gamma band oscillations, therefore provided a measure of the effective or functional connectivity between any pair of output pixels.

2.4. Eigenvalue Analysis

The effective connectivity matrix, each element of which was given by the peak spectral amplitude in the CCH computed between the corresponding 2×2 clusters of ganglion cells, was analyzed to determined its largest eigenvalues and corresponding eigenvectors. The effective connectivity between pairs of output pixels was set identically to zero if the local oscillatory power at either or both image locations did not exceed the gamma-band activity threshold. For the example image analyzed below, the fraction of output pixels exceeding the local gamma band activity threshold was relatively small, so that the resulting functional connectivity matrix was sparse. An additional mask was used to reduce the effective connectivity matrix to only those elements that exceeded a threshold value, set here to 0.425 times the maximum spectral amplitude across all matrix elements. Although the first mask, based on local gamma-band activity, was made redundant by this second mask, the first mask was nonetheless important for computational efficiency because it allowed us to avoid evaluating the CCH between all pairs of output pixels. Sparse matrix analysis methods (Matlab) were used to extract only the 100 largest eigenvalues and corresponding eigenvectors.

3. RESULTS

To explore the dynamic segmentation of gray scale images, we simulated retinal responses to a scene containing several well separated objects, in this case an overhead view of airplanes parked on a runway (fig. 2, top). The picture was taken in a spectral band in which the foreground/background contrast was very high. Ignoring for the moment signals encoded by gamma-band oscillations, the output of the retinal model could be assessed by counting the number of spikes from each output neuron, or ganglion cell, over approximately five seconds of simulated activity (fig. 2, bottom left). This analysis window is longer than typical behavioral time scales, but allowed us to better examine the underlying code in the absence of substantial single trial variability. The convergence from input pixels to ganglion cells in the model was 4:1, accounting for the reduced spatial resolution of the retinal output compared to the input image (128×128 vs. 256×256 pixels, respectively). Due to the contrast enhancement produced by lateral interactions between retinal neurons, faint image features are accentuated in the processed output, resulting in an amplification of fine details despite the reduced spatial resolution. Contrast enhancement via lateral inhibition has long been recognized to be an important aspect of retinal processing[25, 26].

While alpha ganglion cells in the cat retina are known to convey information about local contrast in their mean firing rates[27], the same cells may simultaneously convey additional information in the form of high frequency, or upper gamma-band, modulations. We therefore compared the image reconstructed from the mean spike rate alone with that reconstructed from the gamma band oscillations about the mean firing rate. To magnify the contribution from coherent activity with zero phase lag, the output spike trains were combined into 2×2 arrays of neighboring ganglion cells in which non-phase-locked high frequency components would tend to cancel out. The combined spike trains from the 2×2 clusters of neighboring ganglion cells were Fourier analyzed and the results presented as a filtered image in which the intensity of each pixel was proportional to the peak spectral amplitude in the upper gamma band, between 40 and 120 Hz (fig. 2, bottom right). For comparison, the information conveyed by the mean firing rate is shown at the same resolution, so that both images were 64×64 pixels. Comparing the image reconstructed from a pure rate code with that reconstructed from the local gamma-band activity, it is apparent that coherent oscillations exaggerate large image features at the expense of fine spatial detail.

To read out the dynamic segmentation implicit in the degree of phase locking between different image regions, we performed the following analysis. We began by masking all 2×2 clusters of neighboring ganglion cells (output pixels) whose oscillations exceeded a threshold level, defined as three standard deviations above the mean peak spectral amplitude in the upper gamma-band across all output pixels in the image. CCHs were then computed between every pair of output pixels whose local oscillatory amplitude exceeded this threshold. Finally, each pairwise CCH was Fourier transformed and the peak spectral amplitude in the upper gamma band used to define an effective functional connectivity. The resulting functional connectivity matrix thus represented the degree of phase locking between all pairs of output pixels exhibiting significant local oscillations. When one of both members of a given pair of output pixels did not exhibit significant local gamma-band oscillations, the corresponding functional connectivity was set identically to zero, as were the elements along the diagonal. In addition, all elements of the functional connectivity matrix below 0.45 times the amplitude of the largest element were also set to zero. Thus, the resulting functional connectivity matrix was sparse, allowing a computationally efficient extraction of the eigenvalues and eigenvectors (Matlab).

The eigenvectors associated with the nine largest eigenvalues of the functional connectivity matrix were very consistent with the nine airplanes in the original image (fig. 4, Top). This result is reasonable, since in the limiting case in which a finite functional connectivity only exists between pairs of output pixels belonging to the same airplane, the corresponding functional connectivity matrix would be of block diagonal form. An examination of the eigenvalue distribution reveals a sharp fall off beyond the first nine values (fig. 4, Bottom). A cutoff equal to ½ the amplitude of the largest eigenvalue would have been sufficient to automatically segment the original image into its primary components. It may be possible, in general, to compute an optimal cutoff from an appropriate analysis of the eigenvalue distribution, but we have not explored this issue in detail.

Finally, we consider the segmentation of the same image obtained using a watershed algorithm[28-30] implemented at a single scale appropriate to the objects in the image (fig. 5). For the most part, the watershed algorithm did an adequate job of segmenting the nine airplanes. However, the watershed algorithm also detected one spurious segment, presumably due to the fact that after smoothing, there was sufficient contrast between the segmented region and the adjacent area that it retained its own "identity", whereas the rest of the runway tarmac was smoothed enough to become "homogenized" into one segment.
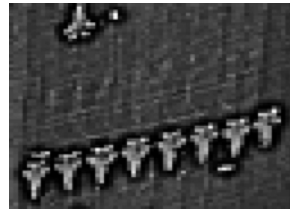
Original Image (256×256)
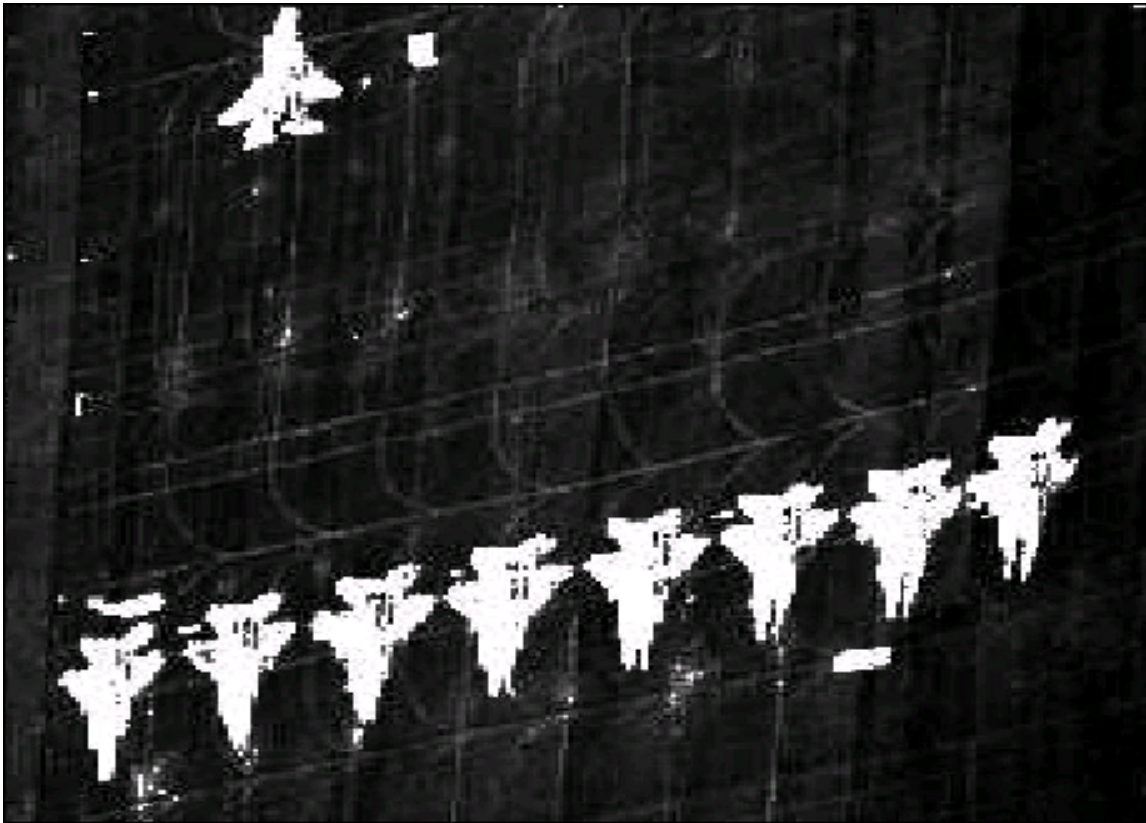
Retinal Output (128×128)

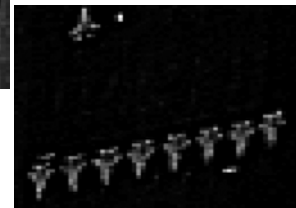Mean Rate
(64×64)

Gamma Band
(64×64)

Fig. 2. Retinal filtering. Top: Original image. Bottom Left: Rate-coded retinal output (1:4 resolution). Pixel intensity proportional to the mean firing rate. Each output pixel represents one ganglion cell. The mean firing rate enhances fine image details. Bottom Right: Information encoded by the mean firing rate vs. information encoded by gamma-band oscillations (1:16 resolution). Local gamma-band activity measured as the peak spectral amplitude between 40-160Hz. Each pixel represents the combined output from a 2×2 array of neighboring ganglion cells. Gamma-band activity enhances large image features at the expense of fine spatial details.

4. DISCUSSION

High frequency oscillatory potentials (HFOPs) are ubiquitous in the vertebrate retina. One clue to their function is the strong stimulus-specificity exhibited by HFOPs recorded simultaneously at separate retinal locations. Here, we have used a computer model to explore the segmentation information implicit in the degree of phase locking between HFOPs evoked by either the same, or by separate, objects. It has been previously shown that the HFOPs produced by the retinal model, which is based on axon-mediated feed back circuits consistent with retinal anatomy, are of the same general frequency, amplitude, and duration—as measured by the persistence of side-peaks in the CCH—as HFOPs recorded experimentally. Moreover, given the high level of synaptic noise in the model, the principal characteristics of phase locking behavior reported here should reflect general dynamical properties of the axon-mediated feedback circuit rather than precise details of the implementation.

The present results affirm our previous observations that model generated HFOPs recorded at separate retinal locations remain phase locked whenever there is a continuous path of stimulated cells between them. This finding suggests that the one topological parameter encoded by phase locked HFOPs is connectedness. In principle, topological information encoded by the degree of phase locking between retinal HFOPs could be read out by downstream neurons. For example, HFOPs arising from simply connected regions of the visual space would add in phase, and thus might produce larger responses than HFOPs arising from non-connected regions, which would add with random phase. Sensitivity to synchronous input has been demonstrated in visual cortical neurons[31], suggesting that retinal HFOPs might contribute to the detection of contiguous features. Retinal HFOPs may also influence the development of intra-cortical connections via spike-timing-dependent-plasticity (STDP)[32]. By causing regions responding to the same object to oscillate in phase, retinal HFOPs may contribute to the development of appropriate feature detectors in the visual cortex.

The main novel finding reported here is that the segmentation information encoded implicitly by the degree of phase locking between separate retinal locations can be explicitly extracted by standard methods for obtaining the eigenvalues and eigenvectors of large, sparse matrices. By using real, as opposed to computer-generated images, we have further demonstrated that the segmentation information implicit in retinal oscillations is not confounded by fine image details. Indeed, HFOPs are not sensitive to fine spatial structure, but rather require big, simply connected, high contrast patches of illumination in order to be strongly activated.
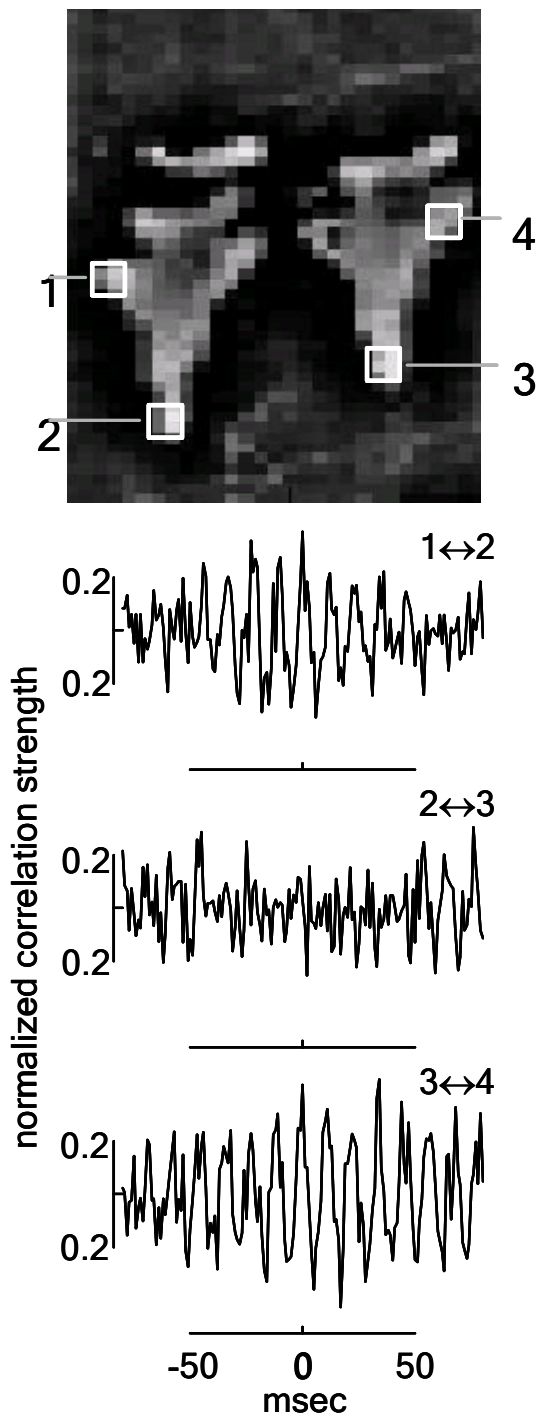

Fig. 3. Dynamic segmentation. Cross-correlation histograms (CCHs) were computed between spike-trains recorded from indicated image regions. Only gamma-band oscillations arising from regions belonging to the same object are phase locked.
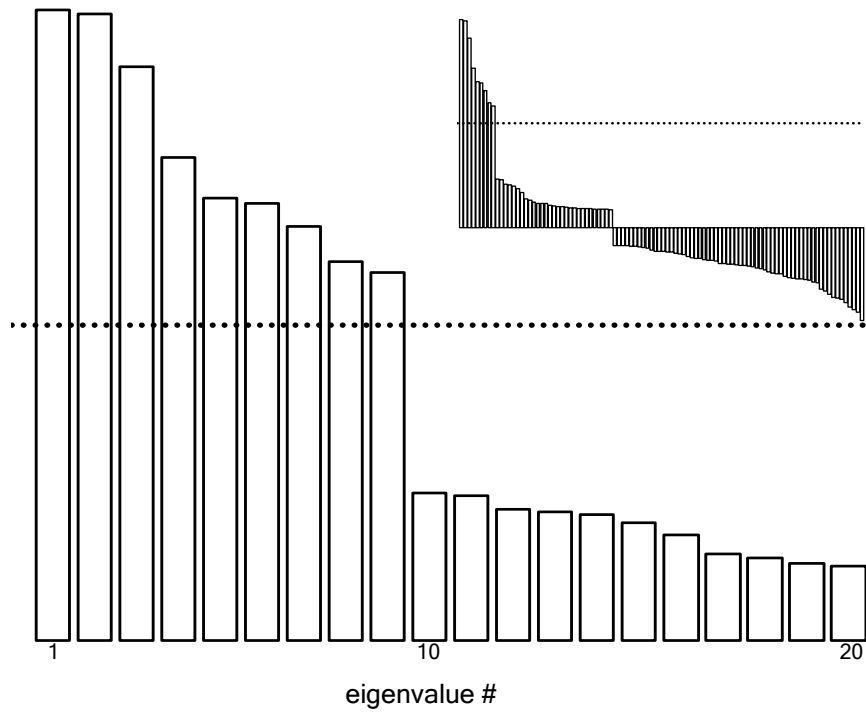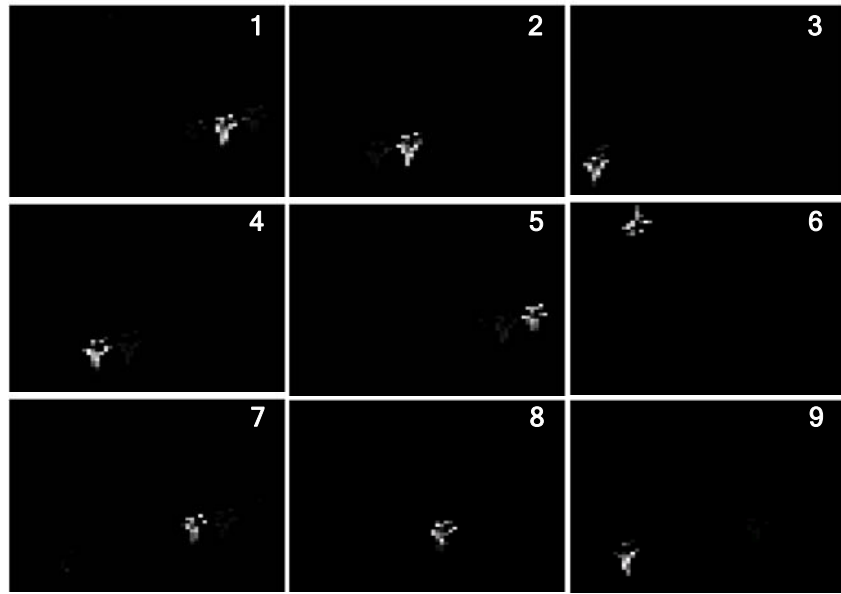
Fig. 4. Eigenvalue analysis of the functional connectivity matrix. Top: Eigenvectors corresponding to the 9 largest eigenvalues of the functional connectivity matrix. Elements of the functional connectivity matrix determined by the peak spectral amplitude in the CCH, computed between every pair of image locations exhibiting significant gamma-band oscillations. Individual eigenvectors, enumerated from largest to smallest, were consistent with the primary objects in the original image. Bottom: Eigenvalue distribution. A bar graph of the largest 20 eigenvalues exhibits a sharp discontinuity between the 9th and 10th eigenvalues. A threshold equal to ½ the amplitude of the largest eigenvalue would have automatically segmented the image into 9 primary objects. Inset: Distribution of the first 100 eigenvalues.

Fig. 5. Watershed Algorithm. A watershed algorithm produced a comparable segmentation of the original image, although a spurious feature on the tarmac was also extracted.

Admittedly, the image we analyzed here did not pose a particularly difficult segmentation problem, consisting as it did of only a few, well-separated objects. Our previous investigations suggest that if a more complex scene had been employed, especially one containing multiple overlapping objects separated by long, low-contrast borders, the segmentation produced by the retinal model would have been significantly worse. The main heuristics the retina uses for accomplishing a dynamic segmentation are size and contiguity. In situations where these simple heuristics are insufficient to distinguish between the individual objects in the scene, the segmentation accomplished by the retina is likely to be correspondingly poor. In higher mammals, it is undoubtedly the job of the visual cortex to segment a more general class of images than can be adequately processed at the level of the retina. Nonetheless, the initial segmentation accomplished by the retina may facilitate subsequent cortical processing.

From a more general point of view, the present results illustrate the application of biological processing strategies to conventional problems in automated image analysis. Although our present findings are based entirely on retinal circuitry, similar phenomena are observed throughout the visual cortex[33]. While the performance of a relatively simple structure, such as the retina, may be only marginally superior to that of conventional image processing technology on a particular task, such as segmentation, it is very likely that models of more complex biological circuits, such as the visual cortex, will exhibit capabilities that far exceed what is currently attainable by engineered systems. Moreover, such biologically based algorithms are naturally parallel, in the sense that the segmentation information is computed in a distributed fashion "simultaneously" across the network, although the extraction of eigenvalues/eigenvectors may be inherently serial.

ACKNOWLEDGEMENTS

REFERENCES

1. M. Ariel, N. W. Daw, and R. K. Rader, "Rhythmicity in rabbit retinal ganglion cell responses," *Vision Research*, vol. 23, pp. 1485-93, 1983.
2. L. J. Frishman, A. W. Freeman, J. B. Troy, D. E. Schweitzer-Tong, and C. Enroth-Cugell, "Spatiotemporal frequency responses of cat retinal ganglion cells," *Journal of General Physiology*, vol. 89, pp. 599-628, 1987.
3. M. Laufer and M. Verzeano, "Periodic activity in the visual system of the cat," *Vision Res*, vol. 7, pp. 215-29, 1967.
4. S. Neuenschwander and W. Singer, "Long-range synchronization of oscillatory light responses in the cat retina and lateral geniculate nucleus," *Nature*, vol. 379, pp. 728-32, 1996.
5. S. Neuenschwander, M. Castelo-Branco, and W. Singer, "Synchronous oscillations in the cat retina," *Vision Res*, vol. 39, pp. 2485-97, 1999.

6. R. H. Steinberg, "Oscillatory activity in the optic tract of cat and light adaptation," *J Neurophysiol*, vol. 29, pp. 139-56, 1966.

7. H. Ishikane, A. Kawana, and M. Tachibana, "Short- and long-range synchronous activities in dimming detectors of the frog retina," *Vis Neurosci*, vol. 16, pp. 1001-14, 1999.

8. L. Wachtmeister and J. E. Dowling, "The oscillatory potentials of the mudpuppy retina," *Invest Ophthalmol Vis Sci*, vol. 17, pp. 1176-88, 1978.

9. L. Wachtmeister, "Oscillatory potentials in the retina: what do they reveal," *Prog Retin Eye Res*, vol. 17, pp. 485-521, 1998.

10. F. De Carli, L. Narici, P. Canovaro, S. Carozzo, E. Agazzi, and W. G. Sannita, "Stimulus- and frequency-specific oscillatory mass responses to visual stimulation in man," *Clin Electroencephalogr*, vol. 32, pp. 145-51, 2001.

11. L. J. Frishman, S. Saszik, R. S. Harwerth, S. Viswanathan, Y. Li, E. L. Smith, 3rd, J. G. Robson, and G. Barnes, "Effects of experimental glaucoma in macaques on the multifocal ERG. Multifocal ERG in laser-induced glaucoma," *Doc Ophthalmol*, vol. 100, pp. 231-51, 2000.

12. N. V. Rangaswamy, D. C. Hood, and L. J. Frishman, "Regional variations in local contributions to the primate photopic flash ERG: revealed using the slow-sequence mfERG," *Invest Ophthalmol Vis Sci*, vol. 44, pp. 3233-47., 2003.

13. G. T. Kenyon and D. W. Marshak, "Gap junctions with amacrine cells provide a feedback pathway for ganglion cells within the retina," *Proc R Soc Lond B Biol Sci*, vol. 265, pp. 919-25, 1998.

14. D. M. Dacey and S. Brace, "A coupled network for parasol but not midget ganglion cells in the primate retina," *Visual Neuroscience*, vol. 9, pp. 279-90, 1992.

15. R. Jacoby, D. Stafford, N. Kouyama, and D. Marshak, "Synaptic inputs to ON parasol ganglion cells in the primate retina," *Journal of Neuroscience*, vol. 16, pp. 8041-56, 1996.

16. D. I. Vaney, "Patterns of neuronal coupling in the retina," *Progress in Retinal and Eye Research*, vol. 13, pp. 301-355, 1994.

17. M. A. Freed and P. Sterling, "The ON-alpha ganglion cell of the cat retina and its presynaptic cell types," *Journal of Neuroscience*, vol. 8, pp. 2303-20, 1988.

18. H. Kolb and R. Nelson, "OFF-alpha and OFF-beta ganglion cells in cat retina: II. Neural circuitry as revealed by electron microscopy of HRP stains," *Journal of Comparative Neurology*, vol. 329, pp. 85-110, 1993.

19. G. T. Kenyon, B. Moore, J. Jeffs, K. S. Denning, G. J. Stephens, B. J. Travis, J. S. George, J. Theiler, and D. W. Marshak, "A model of high-frequency oscillatory potentials in retinal ganglion cells," *Vis Neurosci*, vol. 20, pp. 465-80., 2003.

20. M. Castelo-Branco, S. Neuenschwander, and W. Singer, "Synchronization of visual responses between the cortex, lateral geniculate nucleus, and retina in the anesthetized cat," *J Neurosci*, vol. 18, pp. 6395-410, 1998.

21. D. N. Mastronarde, "Correlated firing of retinal ganglion cells," *Trends in Neurosciences*, vol. 12, pp. 75-80, 1989.

22. G. T. Kenyon, B. J. Travis, J. S. George, J. Theiler, and D. W. Marshak, "Stimulus-specific oscillations in a retinal model," *IEEE Transactions on Neural Networks: Special Issue on Temporal Coding for Neural Information Processing*, in press.

23. M. A. Freed, "Rate of quantal excitation to a retinal ganglion cell evoked by sensory input," *J Neurophysiol*, vol. 83, pp. 2956-66, 2000.

24. G. L. Gerstein and D. H. Perkel, "Mutual temporal relationships among neuronal spike trains. Statistical techniques for display and analysis," *Biophys J*, vol. 12, pp. 453-73, 1972.

25. K. Hartline and F. Ratliff, "Inhibitory interaction of receptor units in the eye of limulus," *Journal of General Physiology*, vol. 40, pp. 1357-1376, 1957.

26. R. W. Rodieck, "Quantitative analysis of cat retinal ganglion cell response to visual stimuli," *Vision Research*, vol. 5, pp. 583-601, 1965.

27. J. B. Troy and C. Enroth-Cugell, "X and Y ganglion cells inform the cat's brain about contrast in the retinal image," *Exp Brain Res*, vol. 93, pp. 383-90, 1993.

28. L. Vincent and P. Soille, "Watersheds in digital spaces: An efficient algorithm based on immersion simulations," *IEEE Trans. on Pattern Analysis and Machine Intelligence*, vol. 13, pp. 583--598, 1991.

29. P. Salembier, "Unsupervised Morphological Segmentation for Images," presented at Proc. of IEEE Winter Workshop on Nonlinear Digital Signal Processing, Finland, 1993.

30. P. Salembier, "Morphological Multiscale Segmentation for Image Coding," *Signal Processing*, vol. 38, pp. 359-386, 1994.
31. J. M. Alonso, W. M. Usrey, and R. C. Reid, "Precisely correlated firing in cells of the lateral geniculate nucleus," *Nature*, vol. 383, pp. 815-9, 1996.
32. H. Yao and Y. Dan, "Stimulus timing-dependent plasticity in cortical processing of orientation," *Neuron*, vol. 32, pp. 315-23., 2001.
33. W. Singer and C. M. Gray, "Visual feature integration and the temporal correlation hypothesis," *Annual Review of Neuroscience*, vol. 18, pp. 555-86, 1995.